GaAs/GaInP nanowire solar cell on Si with state-of-the-art V oc and quasi-Fermi level splitting

Capucine Tong, Amaury Delamarre, Romaric de Lépinau, Andrea Scaccabarozzi, Fabrice Oehler, Jean-Christophe Harmand, Stéphane Collin, Andrea Cattoni

GaAs/GaInP nanowire solar cell on Si with state-of-the-art Voc and quasi-Fermi level splitting

Capucine Tong,[1,2] Amaury Delamarre,[1,2] Romaric De Lépinau,[1,2] Andrea Scaccabarozzi,[1,2] Fabrice Oehler,[1] Jean-Christophe Harmand,[1] Stéphane Collin,[1,2,*] and Andrea Cattoni[1,2,†]

[1]*Centre de Nanosciences et de Nanotechnologies (C2N), CNRS, Université Paris-Saclay, 91120 Palaiseau, France*
[2]*Institut Photovoltaïque d'Ile-de-France (IPVF), 91120 Palaiseau, France*

With their unique structural, optical and electrical properties, III-V nanowires (NWs) are an extremely attractive option for the direct growth of III-Vs on Si for tandem solar cell applications. Here, we introduce a core-shell GaAs/GaInP NW solar cell grown by molecular beam epitaxy on a patterned Si substrate, and we present an in-depth investigation of its optoelectronic properties and limitations. We report a power conversion efficiency of almost 3.7 %, and a state-of-the-art open-circuit voltage (V_{OC}) for a NW array solar cell on Si of 0.65 V. We also present the first quantification of the quasi-Fermi level splitting in NW array solar cells using hyperspectral photoluminescence measurements. A value of of 0.84 eV is obtained at 1 sun (1.01 eV at 81 suns), which is significantly higher than qV_{OC}. It indicates NWs with a better intrinsic optoelectronic quality than what could be expected from TEM images or deduced from electrical measurements. Optical and electronic simulations provide insights into the main absorption and electrical losses, and guidelines to design and fabricate higher-efficiency devices. It suggests that improvements at the n-type contact (GaInP/ITO) are key to unlocking the potential of next generation NW solar cells.

I. Introduction

Tandem solar cells consisting of III-V semiconductor layers with optimal bandgap stacked on top of a conventional Si cell are one of the most promising ways to overcome the Shockley-Queisser efficiency limit for single-junction solar cells of $\sim$ 30 % (1 sun) [1]. The current power conversion efficiency record for Si-based multijunction solar cells is 35.9 % and was obtained by direct wafer bonding and substrate removal[2]. Mismatch in the lattice constant and thermal expansion coefficient between the materials renders the direct growth of high-quality III-V layers on Si difficult and leads to maximum efficiencies of 25.9 %[3].

Owing to their small dimensions, III-V nanowires (NWs) can accommodate both lattice and thermal coefficient mismatches without the introduction of misfit dislocations at the interface [4, 5]. Furthermore, NWs absorb a higher amount of light than their planar counterparts due to light trapping phenomena [6–8]. Numerical simulations indicated a theoretical efficiency of 33.8 % for a tandem GaAsP NW solar cell (1.7 eV) on Si[9]. The simulations were carried out on a NW cell of composition $GaAs_{0.77}P_{0.23}$ in a p-i-n radial structure, taking advantage of the orthogonality between the direction of light absorption and carrier collection, even though the debate about the advantages and disadvantages of axial vs. radial NW junctions is still ongoing [10]. Given that ternary III-V compositions are difficult to control and less studied than binary compounds, most efforts in the photovoltaics community have been focused on fabricating GaAs-based NW solar cells [11–15].

To date, the best GaAs NW on Si tandem solar cell has reached an efficiency of 11.4 %[16], while the best single junction GaAs NW solar cell directly grown on Si has demonstrated an efficiency of 7.7 %[15]. So far, the performances of GaAs NW solar cells grown on Si have been primarily limited by their open-circuit voltage (V_{OC} ¡ 0.62 V for NW array solar cells[15]). Note that in the same study, a V_{OC} of 0.77 V was obtained for a single NW solar cell, however the direct comparison with NW array solar cells is difficult and should consider the fact that a single NW absorbs light from an area, the absorption cross-section, much larger than its geometrical cross-section[7]. The maximum V_{OC} achievable is given by the quasi-Fermi level (qFl) splitting ($\Delta\mu$) generated in the absorber material and related to the density of photogenerated charge carriers[17, 18]. The qFl splitting can be determined from absolute photoluminescence (PL) measurements, and compared to the electrically measured V_{OC} to gain information on the origin of voltage losses in the device[17–24]. Other parameters influencing the performance of a NW solar cell include the NW crystal quality, vertical yield, doping concentration and surface passivation[25].

While a good NW crystal quality is essential to make a performant solar cell, it is common to find a high density of stacking faults in self-catalyzed GaAs NWs due to crystal phase mixing [26–28]. Ensuring a high yield of vertical NWs is also critical and several studies have been dedicated to its optimization [29–37]. Studies show that the various substrate preparations and growth parameters controlling the NW growth direction make it difficult to obtain reproducible results. However, studies have shown empirically that GaP NW arrays systematically present higher vertical yields than GaAs NW arrays[35, 38], and that growing a GaP stem prior to GaAs NW growth can enhance the yield of vertical NWs[14, 27, 37, 38]. Nevertheless, the presence of a valence band (VB) offset between the GaP and the Si may introduce an additional barrier for hole extraction, and its impact on NW solar cell performances has not yet been investigated.

Semiconductor doping is key to functional p-n junctions, however the introduction of dopants during NW growth greatly affects the thermodynamics and kinetics of the sys-

* stephane.collin@c2n.upsaclay.fr
† andrea.cattoni@c2n.upsaclay.fr

tem often resulting in axial and radial doping gradients in NWs [39–43]. Doping compensation mechanisms can also prevent high doping concentrations to be achieved [44–46], rendering surface passivation essential for most III-V NWs. This is important for GaAs NWs as they are particularly prone to surface depletion due to high surface recombination velocity [47–52].

Finally, all NWs need to be ohmically contacted to efficiently extract charge carriers from the solar cell. Indium tin oxide (ITO) is often used as a transparent conductive oxide (TCO) to collect the electrons while minimizing shadowing effects. But its interface with GaAs or GaInP has been shown to form an important Schottky barrier [53–57], hindering the overall device performance.

In this work, we present a GaAs/GaInP NW solar cell directly grown on Si by molecular beam epitaxy (MBE). Current-voltage measurements of the cell indicate a V_{OC} of 0.65 V, which is at the state-of-the-art for a NW array solar cell on Si. Hyperspectral photoluminescence measurements evidence a qFl splitting of 0.84 eV, significantly higher than qV_{OC}, indicating good optoelectronic quality NWs. The various reasons behind the lower qV_{OC} are discussed. Optical and electronic simulations are used to study the main absorption and electrical losses.

II. Experimental

A. Selective area growth of III-V nanowire arrays on Si

1. *Patterned substrate preparations.*

In this study, one-sixth of a two-inch p-doped (B) Cz Si(111) wafer supplied by Siltronix is used (nominal resistivity: 0.010.02 Ω cm). The surface is cleaned by three successive cycles of oxidation in oxygen plasma reactive ion etching (RIE) and etching in hydrofluoric acid (HF) diluted in water to 5 % concentration. A 37 1 nm thick silica layer is deposited via plasma-enhanced chemical vapor deposition (PECVD). The substrates are coated with an electron-sensitive resist (495PMMA, 2 %) and patterned in a Vistec EBPG 5000+ electron beam lithography machine, operating at 100 kV, resulting in a hexagonal array of holes with a 500 nm pitch. This hole pattern is transferred into the SiOx layer by capacitively coupled plasma-reactive ion etching (CCP-RIE) at 7 mTorr, with a mixture of SF_6 and CHF_3 gases (flow rate ratio of 8:20) and a bias voltage of 190 V. To avoid plasma-induced damage and amorphization of the first Si layers, about 4 nm of SiOx is left inside the holes. The PMMA resist is removed by successive immersion in trichloroethylene and acetone with sonication, then rinsed with isopropanol. To ensure complete removal of organic residues, the sample is then subjected to an oxygen plasma cleaning by CCP-RIE. The remaining SiOx inside the holes is removed by a dip in a 1 % HF solution (diluted in water), during 30 s. After rinsing with de-ionized water and drying with N_2, the sample is stored overnight in a box filled with N_2 before being transported the next day to a Riber32 MBE chamber. The substrate is outgassed in the preparation chamber at 500-550 C until a pressure of 3 x 10^{-9} Torr is reached.

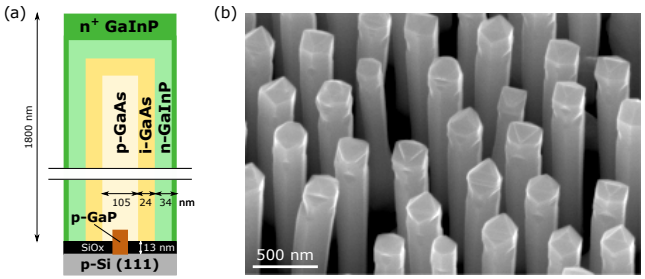

Figure 1 (a) Schematic of the dimensions of a core-shell GaAs/GaInP heterojunction NW with a delta-doped GaInP capping layer. (b) Tilted (35°) SEM overview of an as-grown GaAs/GaInP NW array with a 500 nm pitch.

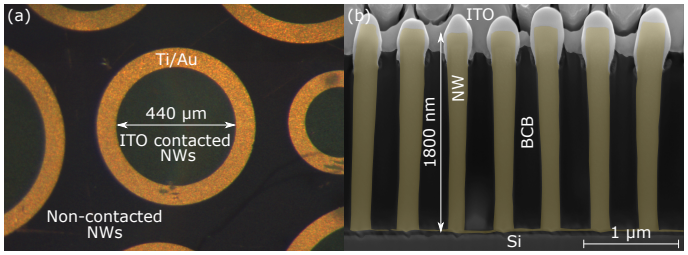

Figure 2 (a) Top view stereo microscope image of the NW solar cell presented in this study. (b) Tilted (45) SEM image of the same cell, showing its different layers. The as-grown NWs are colored in yellow, while the Si substrate, BCB matrix and ITO are uncolored and can be easily distinguished.

2. *Epitaxy of GaAs/GaInP core-shell NW arrays.*

Prior to growth, the substrate is held at 690 10 C for 10 min in the MBE growth chamber on a rotating holder (typically 10 rpm), after which the growth temperature is stabilized at 620 ± 5 C as monitored with a 0.9 μm IRCON pyrometer. The growth procedure is initiated by a 1 min Ga pre-deposition with an equivalent thickness of 42 monolayer (ML) GaAs(100), and a Be flux of 6 x 10^{11} cm^{-2} s^{-1}. A Be-doped GaP stem (p-GaP) is grown during 80 s at a P_2/Ga flux ratio of 1, before linearly closing the P valve while opening As over 30 s. This results in a linearly graded GaP/GaAs transition which contributes to flatten the VB offset between GaP and GaAs[14]. The main Be-doped GaAs core segment (p-GaAs) is then grown under an As_4/Ga flux ratio of 1.2, and the same Be flux during 12 min. The Ga flux during the GaP stem and GaAs core growths is set to correspond to a 2 Å s^{-1} growth rate on GaAs(100). The liquid Ga catalyst droplet is then consumed in situ during 20 min at the same temperature by shutting down the Ga flux and using an As_4 flux at 16 % of its value during core growth. A nominally intrinsic GaAs shell (i-GaAs) is grown during 30 min at a substrate temperature of 590 ± 10 C under a Ga flux of 0.74 Å s^{-1} and an excess of As_4 (As_4/Ga flux ratio of 7.1). The substrate temperature is finally set to 470 ± 10 C for the 25 min growth of a Si-doped GaInP shell (n-GaInP), aiming at a

planar growth rate of 1.1 Å s^{-1}, a planar composition of $In_{0.58}$ $Ga_{0.42}P$ and a planar doping level of 6 x 10^{18} cm^{-3}. The NW structure is terminated by an n-type delta-doped GaInP capping layer (n^+-GaInP). GaInP is grown during 32 s before stopping the Ga and In flux and providing an increased Si flux under excess P_2 for another 32 s, resulting in a Si surface concentration of 1.4 x 10^{12} cm^{-2} in one atomic plane. This cycle is repeated 10 times, resulting in an equivalent GaInP layer grown during 5.35 min with an average Si concentration of 1.7 x 10^{19} cm^{-3}.

3. Characterization of as-grown NW arrays.

From the scanning electron microscope (SEM) image of the as-grown NW array (Figure 1b), the NWs height and diameter could be determined as h_{NW} = 1800 130 nm and D_{NW} = 220 20 nm, respectively. The p-GaAs NW core diameter reported in Figure 1a was obtained from the measurement of NW cores previously grown in nearly identical conditions. The i-GaAs shell thickness was deduced by subtracting the p-GaAs NW core diameter from the total width of the As-containing region, as determined by cross section Energy-Dispersive X-ray spectroscopy (EDX), see Figure 6 in the appendix. Similarly, the GaInP shell thickness was determined from the lateral extension of the (In,P)-containing regions of the cross-section EDX maps. Note that these EDX-determined shell thicknesses are rough estimates and significant errors are expected due to several factors. First, the diffusion dynamics of group III adatoms vary depending on the species and the growth temperature. Some regions in the shell may collect more or less material due to shadowing of surroundings NWs, resulting in non-uniform thickness. Furthermore, the NW core diameter is also found to vary between growths and after droplet consumption (typically within 20 nm). Finally, the geometrical surface orientation relative to the angle of the MBE cell leads to severe growth rate differences between the NW head and sidewall, as much as a factor of six, as measured by Transmission Electron Microscopy (TEM), see Figure 6 in the appendix. On average the GaInP NW sidewalls are found to be richer in Ga, which is why we correct the nominal target Ga fraction to $Ga_{0.42}In_{0.58}P$, instead of using the theoretical GaAs-matched composition of $Ga_{0.51}In_{0.49}P$. Quantitative EDX analyses of the Ga content variation in the GaInP shell can be found in Figure 7 in the appendix. Extended defects such as dislocations and twins are also visible on the scanning TEM image in Figure 6 in the appendix.

The doping levels are estimated in the core and shell of previous GaAs NW samples grown in similar conditions using cathodoluminescence (CL) spectroscopy by fitting the spectrum to a generalized Planck law, as described in our earlier work[46, 58]. The core p-type doping with Be is thus expected here to be close to p = 5 10^{18} cm^{-3}, whereas the shell n-type doping with Si is limited to n ¡ 1 10^{18} cm^{-3} [46]. The size and carrier concentration of the p-GaP stem are difficult to measure. Estimations from growth parameters suggest a roughly 80 nm long and 40 nm wide p-GaP stem with a doping concentration similar to the one in the p-GaAs core. Potential hole extraction barriers in the processed NW device arising from the introduction of this additional heterojunction at the foot of the NW are discussed in section 5.

B. Nanowire solar cell fabrication

The as-grown NWs are embedded in a BCB matrix (Cyclotene 3022-46) for planarization. Plasma CCP-RIE etching and a dip in 1 % HF follow to reveal the NW heads. Photolithography is then used to deposit 150 nm of ITO and Ti/Au contacts on specific areas of the sample to electrically connect NWs of the same cell and ensure good mechanical and electrical contact with measurement probes. The back contact is formed by depositing a 300 nm Al layer on the p-Si(111) wafer. The final device is made up of several circular cells with diameters ranging from 140 m to 1 mm. The champion cell, on which this article will be focused, is shown in Figure 2a. It has an outer diameter of 600 m and an inner diameter of 440 μm. After characterization, a cross section view of the same cell is obtained by Focused Ion Beam (FIB) milling and tilted SEM imaging (Figure 2b).

III. Optoelectronic properties

A. Current-voltage (JV) characteristics

The electrical performances of 13 NW solar cells are measured using a Keithley 2601B source measure unit in a two-probe configuration at room temperature, in the dark and under a 1-sun illumination. The latter is provided by a Newport 94011A-ES solar simulator equipped with an AM1.5G filter. The recorded open-circuit voltage (V_{OC}), short-circuit current (J_{SC}), fill factor (FF) and efficiency values are summarized in the appendix (Figure 8). The JV characteristics of the champion cell in the dark and under a 1-sun illumination are shown in Figure 3a. A high V_{OC} of 0.65 V is obtained, along with a J_{SC} of 15.5 mA/cm^2 and FF of 40 %. External quantum efficiency (EQE) integration across the relevant wavelength range (Figure 3c) resulted however in a J_{SC} value of 14.2 mA/cm^2. The latter will be the official J_{SC} value reported as J_{SC} determination from EQE has the advantage of being independent of the spectral shape of the light source, unlike J_{SC} determination from J-V measurement. The resulting power conversion efficiency of 3.68 % is at the state-of-the-art of solar cells with GaAs-based radial junction NWs grown on Si [14, 27]. However, the performances of this NW solar cell are still far behind the ones of the best GaAs thin film solar cells. The cross-over between the dark and the illuminated curves at 0.7 V suggests an electron barrier in the conduction band which is reduced upon photodoping. The slope of the illuminated JV curve near the short-circuit current point indicates either an incomplete collection of charge carriers, or a low shunt resistance which reduces the amount of current flowing through the solar cell junction. The semi-logarithmic plot of the JV curve in the dark is shown in Figure 3b along with a one-diode model fit. A high and unfittable reverse-current can be observed, while the forward current is accurately fitted with a high ideality factor of 4 and a recombination parameter of J_0 = 4.1 10^{-6} A cm^{-2}. Satisfying shunt and series resistance of 7.2 10^3 Ω cm^2 and 0.17 Ω cm^2, respectively, were also fitted from the forward current.

B. External quantum efficiency

A custom-built setup is used to measure the EQE of the NW solar cell. Light emitted by a Xenon lamp is filtered using a grating monochromator and guided to the setup optical axis with an optical fibre. The photon flux over the spectral range of interest is first calibrated with a reference Si diode with known responsivity. Then, the sample is subject to the same illumination conditions, while the current at its terminals is collected at zero bias with a Keithley 2600 source measure unit. The resulting EQE of the NW cell is shown in Figure 3c. Between 700 and 800 nm the EQE remains relatively constant around 60 % and is higher than the EQE values measured in other radial junction GaAs-based NW solar cells[14, 27]. Below 700 nm the EQE decreases steadily, although experiments showed that a high-temperature annealing could increase the short wavelength part of the EQE by improving contact conductivity[38]. Due to light scattering, specular reflectivity measurements could not be used to explicitly differentiate absorption issues from carrier collection issues, so simulations of the absorption in the different regions of the NW solar cell are carried out.

C. NW absorption modelling.

A frequency-domain modal method known as the Rigorous Coupled-Wave Analysis (RCWA) [59–62] is used to model the absorption in the GaAs NWs, the GaInP contact and the ITO layer. A top view of the unit cell (hexagonal lattice) used to generate the NW array solar cell in the simulations is shown in the appendix in Figure 9 (left). A cross-section view of the simulated NW solar cell along a single NW is also shown in Figure 9 (right).

The simplified design incorporates the main elements of the NW solar cell previously presented, with the GaInP segment only present at the top of the NW as it is six times thicker than the GaInP shell and is expected to be the main source of photon absorption in GaInP. A more refined design is not justified also due to the morphology dispersion between the different NWs of the NW array composing the cell.

The absorption in each material (Figure 3c, dashed curves) is calculated using 20 Fourier orders and the optical constants used for the RCWA simulations are plotted in Figure 10 in the appendix. The simulated absorption in the GaAs NWs (brown) is slightly higher than the experimentally measured EQE of the solar cell (red), although the general trend of the EQE is well reproduced by the simulations. The calculated short-circuit current, assuming that all the photo-generated carriers are collected, is 18.77 mA/cm^2. The difference of about 4.5 mA/cm^2 may be due to a non-perfect carrier collection or to an underestimation of the parasitic absorption inside the GaInP contact and/or the ITO. The parasitic absorption inside the GaInP contact is relatively high (2.84 mA/cm^2) even without considering the 34 nm-thick GaInP shell in the simulations.

The performances of the NW solar cell presented could be hindered by poor crystalline quality NWs, defective interfaces and contacts both at the foot (interface between the GaP stem and the Si substrate) and at the top of the NWs (contact between the GaInP shell and the ITO). As high optoelectronic quality NWs are essential for a performant solar cell, hyperspectral PL is used to assess the quasi-Fermi level splitting developed in the NWs under illumination. The latter has been shown to represent the maximum V_{OC} that a solar cell can achieve [17, 18], and is discussed in the following section.

IV. Absolute photoluminescence (PL) and quasi-Fermi level (qFl) splitting

To better assess the optical properties of the NWs, a spatially and spectrally resolved hyperspectral imager set-up calibrated in absolute units is used [17]. LED excitation at 450 nm is carried out through a microscope objective with numerical aperture (NA) 0.6. Measurements are performed at illumination intensities varying from below 1 sun to 81 suns. The measurement at 12 suns is carried out with a 532 nm laser due to a set-up change.

According to the generalized Planck law, the absolute photon flux (ϕ_{PL}) emitted from a semiconductor under illumination into a hemisphere above its flat surface can be related to the carrier temperature (T) and the qFl splitting ($\Delta\mu$), assuming the latter is constant (equation 1). The qFl splitting of a material has previously been shown to correspond to the maximum achievable V_{OC} of the device [17, 18]. Here, $A(\hbar\omega)$ is the absorption probability of an incident photon of energy $\hbar\omega$ on a surface element, $\hbar$ the reduced Planck constant, c the speed of light in vacuum and k_B the Boltzmann constant. The absolute photon flux ϕ_{PL} is expressed as:

$$\phi_{PL} = \frac{A(\hbar\omega)}{4\pi^2\hbar^3c^2}\frac{(\hbar\omega)^2}{exp(\frac{(\hbar\omega)-\Delta\mu}{k_BT})-1}. \quad (1)$$

This equation assumes an entirely collected Lambertian emission profile which has been shown to be an accurate description of the angular emission profile of non-optimized NW arrays [63]. In non-degenerate semiconductors where the Fermi levels lie a few kT away from the band edges, the Fermi distribution can be approximated by a Boltzmann distribution:

$$\phi_{PL} = EQE(\hbar\omega)\frac{(\hbar\omega)^2}{4\pi^2\hbar^3c^2}exp(\frac{-\hbar\omega}{k_BT})exp(\frac{\Delta\mu}{k_BT}). \quad (2)$$

In this equation, the absorption probability A($\hbar\omega$) has been approximated by the EQE($\hbar\omega$), since only the latter can be experimentally measured. We consider this approximation to be reasonable considering the good match between the EQE and the modeled A($\hbar\omega$) in Figure 3c. The semi-logarithmic plot in Figure 4a shows the absolute photoluminescence spectra of the cell under a 12 suns and 81 suns illumination (dashed curves) after averaging the hyperspectral PL images over an area of roughly 50 x 50 μm^2. Figures 11a and 11b in the appendix present the hyperspectral PL maps of the champion cell emission at 870 nm, under an illumination of 12 suns and 81 suns, respectively. Figures 11c and 11d depict the qFl splitting

maps of the same areas obtained by fitting the PL spectra using the generalized Planck law (equation 2) between 1.43 and 1.52 eV, with a fixed carrier temperature of 330 K. Quasi-Fermi level splitting variations of less than ± 30 meV can be observed across the maps, demonstrating the relatively high qFl splitting homogeneity over the characterized device surface. The solid curves in Figure 4a correspond to the PL spectra divided by the cell's EQE (from Figure 3c), while the red lines are their generalized Planck law fit. The $\Delta\mu$ obtained under a 12 suns and 81 suns illumination are 0.95 eV and 1.01 eV, respectively. These two data points are indicated in light blue and cyan, respectively, in Figure 4b.

Due to lower signal-to-noise ratio at weaker illumination intensities (i 12 suns), instead of directly measuring spectrally resolved images we measured simple luminescence images, that integrate all wavelengths above the 850 nm long-pass filter, therefore presenting more intense signals. This way we obtain the relative variation of the luminescence from the 81 suns illumination down to 0.7 sun, which is proportional to $exp(\frac{\Delta\mu}{k_BT})$ according to equation 2. Since $\Delta\mu$ was determined to be 1.01 eV at 81 suns, $\Delta\mu$ for lower illuminations can be deduced, as displayed in Figure 4b (dark blue squares). After interpolation, a qFl splitting of 0.84 eV is determined for a 1 sun illumination. This qFl splitting value is considerably higher than the measured qV_{OC} at 1 sun (black squares in Figure 4b), and to the best of our knowledge constitutes a first-time quantification of the qFl splitting in NW array solar cells. Furthermore, as here the qFl splittings are determined by using a generalized Planck law fit in which the absorption probability A($\hbar\omega$) is approximated by the EQE($\hbar\omega$) (equation 2), the resulting qFl splitting values are lower limits. Upper limits of the qFl splittings can be deduced by using a 30 % higher absorption, as obtained from the optical simulations in section 3.3. The latter would translate into an 8 meV increase in the qFl splitting values ($kT\ ln(1.3)$, where T = 330 K). The ideality factors $n_{\Delta\mu}$ and $n_{V_{OC}}$ indicated in Figure 4b are obtained by fitting the slope of the variation of $\Delta\mu$ and V_{OC}, respectively, with illumination intensity and they are discussed at the end of this section. The high qFl splitting of 0.84 eV at 1 sun indicates a better optoelectronic quality than what could be deduced from electrical measurements and TEM observations alone. It also evidences significant room for device improvement, which can only be achieved if the mismatch between the qFl splitting and the qV_{OC} is clarified.

A first reason could be inhomogeneous NW properties. Let us consider a situation where the NWs can be grouped into two distinct families: family 1 and family 2. In family 1, the NWs sustain a qFl splitting $\Delta\mu_1$, and emit a luminescence signal $A\phi_{bb}exp(\frac{\Delta\mu_1}{k_BT})$. In family 2, the NWs present a negligible qFl splitting $\Delta\mu_2$, and emit a negligible luminescence. Such a situation relies on two assumptions: (i) The effective carrier lifetimes of both NW families are significantly different. (ii) Resistances or current barriers must be present in between NWs, which could originate from processing issues, e.g. local incomplete BCB removal or inhomogeneous TCO deposition. Otherwise, the qFl splitting of each individual NW would equal its voltage, and the voltage of both NW families would equilibrate. It is possible that points (i) and (ii) are true for our solar cells, as they have been observed in similar NWs (VLS grown GaAs NWs on Si) by atomic force microscopy (AFM)[64] and electron beam induced current (EBIC) measurements [65], and in GaN/InGaN core-shell NWs by scanning photocurrent microscopy (SPCM)[66]. Therefore, $\Delta\mu_1$ and $\Delta\mu_2$ can differ, as well as their luminescence emissions. Nevertheless, they cannot be distinguished by luminescence imaging, since the NW-to-NW distance is in the order of the diffraction limit (500 nm). The luminescence density recorded on an area comprising an equal number of NWs from families 1 and 2 will be an average of their respective emission, i.e. $A\phi_{bb}exp(\frac{\Delta\mu_1}{k_BT}) \times 0.5 \approx A\phi_{bb}exp(\frac{\Delta\mu_1 - 20\,\mathrm{meV}}{k_BT})$. This means that the determined qFl splitting (here $\Delta\mu_1 - 20\,\mathrm{meV}$) is close to its highest value. Simultaneously, the voltage can take any value in between $\frac{\Delta\mu_1}{q}$ and $\frac{\Delta\mu_2}{q}$, depending on the local resistances. In the extreme situation where NWs 1 are totally disconnected and NWs 2 are connected without resistance, we have $V = \frac{\Delta\mu_2}{q}$. In the opposite case (NWs 1 connected, NWs 2 disconnected), $V = \frac{\Delta\mu_1}{q}$.

The fact that the qFl splitting obtained (0.84 eV) is higher than the measured qV_{OC} of the cell (V_{OC} = 0.65 V, qV_{OC} = 0.65 eV) could also be due to additional recombinations at heterointerfaces. This has been observed in other types of solar cells, e.g. CIS [67], CIGS [68, 69] or perovskites [70]. In our case, the efficient extraction of the majority charge carriers may be prevented by the p-Si/p-GaP/p-GaAs heterointerface at the foot and by the i-GaAs/n-GaInP/ITO heterointerface at the top, and they may recombine at the dislocations near the i-GaAs/n-GaInP interface introduced due to GaInP shell composition variation along the NW axis. More details on charge generation, separation, recombination and collection could be obtained by using for example two-photon induced photocurrent and photocurrent-voltage responses[71].

The difference in the ideality factors obtained from the variation of $\Delta\mu$ and V_{OC}, respectively, with illumination intensity (for more information on the ideality factors' determination please refer to page 51 of the book by D. Abou-Ras et al.[72]) could also be explained by inhomogeneous NW properties and/or the presence of potential barriers at interfaces and recombination currents. As the ideality factor provides insight on the location of the dominating recombination mechanism in a solar cell[73], the higher ideality factor $n_{V_{OC}}$ = 2.6 compared to the optical ideality factor $n_{\Delta\mu}$ = 1.4 suggests the presence of an additional recombination channel at the GaAs absorber interfaces. However, these ideality factors are still lower than the one obtained from a one-diode model fit of the dark current-voltage characteristics of the cell (n = 4, Figure 3b), and further studies are required to elucidate this matter.

V. Modelling hole transport at the p-type contact

The GaP stem introduced at the p-type contact of the NW structure (brown in Figure 1a) to enhance the vertical yield of the NWs is an additional heterostructure which could be a barrier for hole extraction [75]. To study the impact

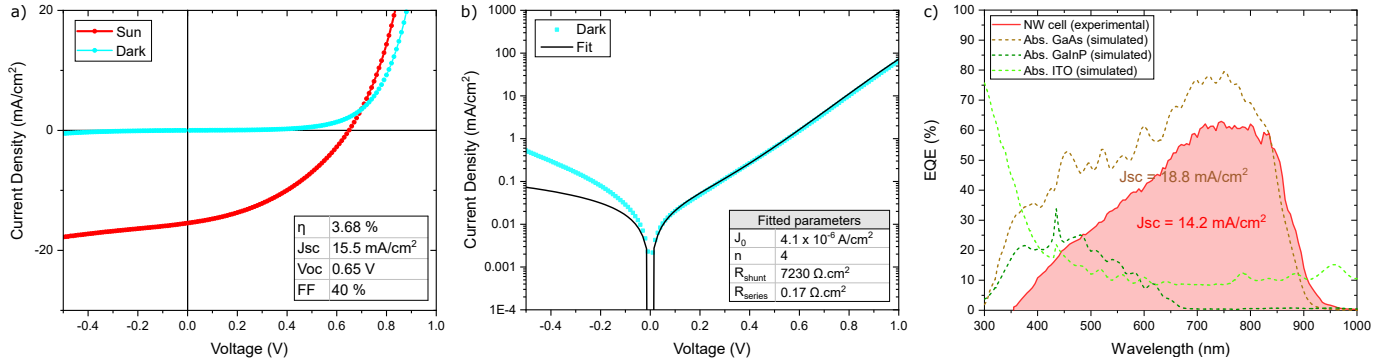

Figure 3 (a) JV curves in the dark (blue) and under a 1 sun illumination (red), (b) semi-logarithmic plot of the JV curve in the dark (blue), along with a one-diode fit (black). (c) EQE of the GaAs/GaInP NW solar cell (red) and simulated absorptions for GaAs, GaInP and ITO (dashed) using the simplified design shown in Figure 9 in the appendix.

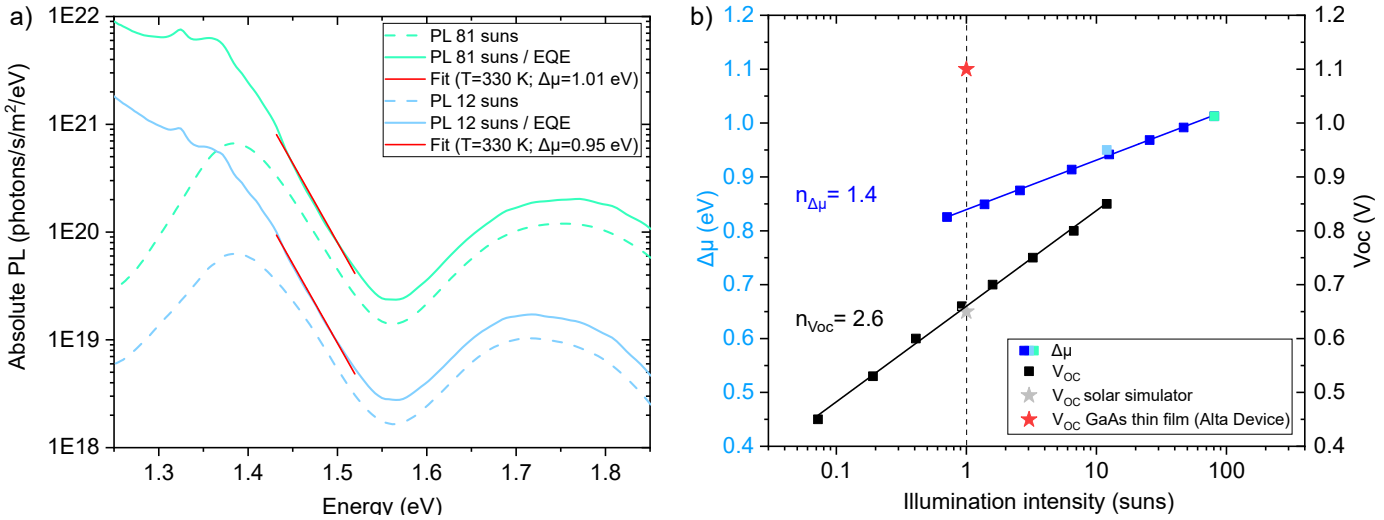

Figure 4 (a) Absolute PL spectrum of the solar cell from Fig. 2 under an illumination of 12 suns and 81 suns (dashed curves). The PL spectra were averaged over a cell area of roughly 50 x 50 μm^2. The same spectra divided by the cell's EQE from Fig. 3c are also shown (solid curves), along with their generalized Planck law fit carried out between 1.43 - 1.52 eV (red lines). (b) Evolution of the quasi-Fermi level splitting ($\Delta\mu$, blue) and the open-circuit voltage (V_{OC}, black) with illumination intensity. The light blue and cyan squares correspond to qFl splittings obtained from spectrally resolved luminescence images, while the dark blue squares are obtained from simple images that integrate all wavelengths. The record V_{OC} for planar GaAs cell (red star) corresponds to the one obtained by Alta Devices [74]

of this barrier, we simulated a simplified one-dimensional structure of the cell previously presented, using the solar cell device simulator SCAPS[76]. Since charges in the NWs are separated radially, the modelled structure illustrated at the top of Figure 5a first follows the NW axis and then the direction perpendicular to the NW axis. Figure 5a presents the simulated band diagrams of the modelled structure under a 1 sun illumination and an applied bias corresponding to the maximum power point (V_{MPP}), for different acceptor doping concentrations in the GaP stem, ranging from 1×10^{18} cm^{-3} to 8×10^{18} cm^{-3}. All band diagrams have been shifted such that the conduction bands (Ec) are aligned on the n-GaInP side. The parameters used in the SCAPS simulations are detailed in Table I in the appendix.

The VB offset (ΔE_V) at the GaP/Si interface directly impacts the simulation results, however its experimentally determined value varies significantly in the literature (from 0.6 eV[77] to 1.1 eV[78]). An average ΔE_V of 0.9 eV was used in the simulations presented in this section (corresponding to a GaP electron affinity of 3.8 eV[79]). The simulation results obtained using the lower and upper bound VB offset values found in the literature are shown in Figure 12 in the appendix.

As observed in Figure 5a, the increase of acceptor doping concentration in GaP brings about a narrowing of the VB potential barrier there. This is also evidenced by the current-voltage curves in Figure 5b through the improved V_{OC}, fill factor, and hence efficiency, with increased dop-

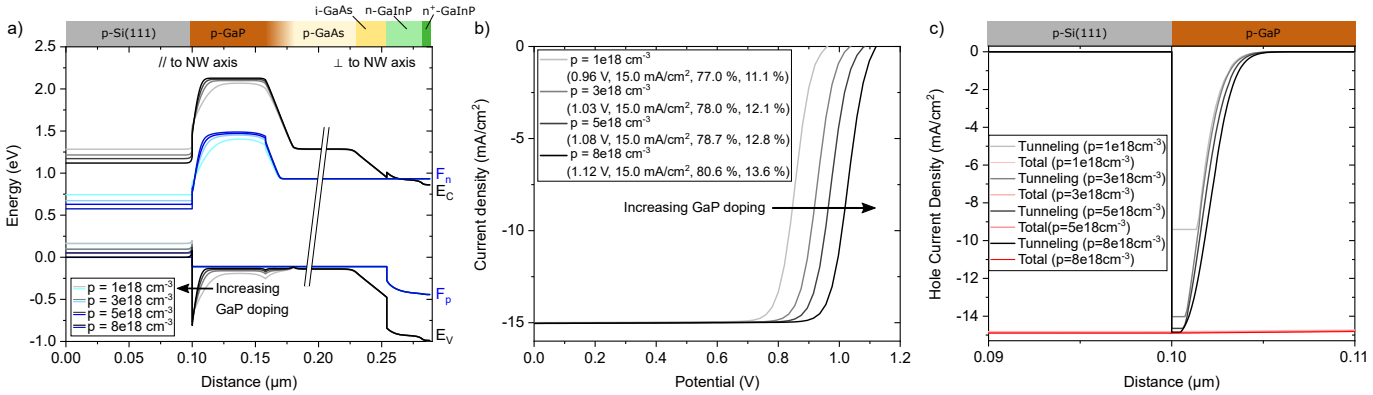

Figure 5 (a) Band diagrams obtained from 1D SCAPS simulations under 1 sun illumination and V_{MPP} bias for different GaP acceptor doping concentrations. (b) Current-voltage characteristics (values in brackets correspond to V_{OC}, J_{SC}, FF, and η) and (c) hole current densities obtained from the same SCAPS simulations.

ing concentration. In fact, as the potential barrier width in GaP is decreased with increasing doping concentration, hole tunnelling becomes more efficient. This is illustrated in Figure 5c where the current density of intra-band tunnelling holes at V_{MPP} (grey/black curves) is almost doubled at the GaP/Si interface when the doping concentration changes from 1×10^{18} cm^{-3} (light grey) to 8×10^{18} cm^{-3} (black). For a doping concentration above 5×10^{18} cm^{-3}, the hole tunnelling current densities (two darkest curves) become comparable to the total hole current density (red lines), indicating that a high doping concentration can help overcome the VB potential barrier in GaP thanks to intra-band tunnelling. The more efficient transport of holes via intra-band tunnelling can also be observed in the band diagrams in Figure 5a, through a lower potential drop across the GaP/Si interface. The doping concentration required for holes to predominantly tunnel through the potential barrier depends on the GaP/Si VB offset (Figure 12 in the appendix), making it difficult to determine a target threshold doping concentration. If the GaP/Si VB offset is closer to the lower bound value of 0.6 eV from the literature[77], then simulations show that the solar cell's performances will not vary much when the GaP doping concentration is increased from 1×10^{18} cm^{-3} to 8×10^{18} cm^{-3}. However, the greater the GaP/Si VB offset the more the cell's performances will be impacted by the GaP doping concentration, as seen in Figures 12c and 12d in the appendix.

It is difficult to precisely determine the size of the actual GaP stem in the NW structure and its doping concentration. However, previous CL studies [46] have shown that the Be doping concentration in our GaAs NW cores, which are grown via the same VLS mechanism, can be superior to 5×10^{18} cm^{-3}. It is thus reasonable to assume that the doping level in the GaP stem is similar and hence that with a GaP/Si VB offset between 0.6 - 1.1 eV, the potential barrier in the VB does not significantly impact hole extraction at the p-type contact in our devices.

VI. Conclusions

A core-shell GaAs/GaInP NW solar cell directly grown on Si by MBE was successfully fabricated. The cell demonstrated a PCE of almost 3.7 % and a state-of-the-art V_{OC} of 0.65 V. A quasi-Fermi level splitting of 0.84 eV at 1 sun (up to 1.01 eV at 81 suns) was determined from hyperspectral PL measurements, which is considerably higher than qV_{OC}. This indicates NWs of good optoelectronic quality and significant room for the improvement of our devices. Numerical 1D simulations showed that the potential barrier at the p-type contact can be overcome if the GaP stem is sufficiently doped. As we expect the hole concentration in the GaP stem to reach 5×10^{18} cm^{-3}, we are confident that our NW solar cell's performances can be further enhanced by improvements at the n-type contact (GaInP/ITO).

Conflicts of interest

The authors declare no conflicts of interests.

Acknowledgements

The authors thank G. Patriarche for STEM-EDX images, L. Largeau for cross-sectional sample preparation by FIB, and Ombeline Lafont, Baptiste Brenguier and Hao Xu for their contribution to early photoluminescence experiments. The authors also thank C. Cornet for insights on the GaP/Si valence band offset values.

The authors acknowledge financial support from the French RENATECH network and the French government in the framework of the Programme dInvestissement dAvenir (ANR-IEED-002-01) and the ANR projects Nanocell (ANR-15-CE05-0026) and PIANIST (ANR-21-CE09-0020-03). This work was also partly funded in the frame of the EMPIR 19ENG05 NanoWires project. The EMPIR (European Metrology Programme for Innovation and Research) initiative is co-funded by the European Union's Horizon 2020 research and innovation programme and the EMPIR Participating States.

[1] W. Shockley and H. J. Queisser, *Journal of Applied Physics*, 1961, **32**, 510–519.

[2] P. Schygulla, R. Müller, D. Lackner, O. Höhn, H. Hauser, B. Bläsi, F. Predan, J. Benick, M. Hermle, S. W. Glunz and F. Dimroth, *Progress in Photovoltaics: Research and Applications*, 2022, 869–879.

[3] M. Feifel, D. Lackner, J. Schön, J. Ohlmann, J. Benick, G. Siefer, F. Predan, M. Hermle and F. Dimroth, *Solar RRL*, 2021, **5**, 2000763.

[4] L. C. Chuang, M. Moewe, C. Chase, N. P. Kobayashi, C. Chang-Hasnain and S. Crankshaw, *Applied Physics Letters*, 2007, **90**, 043115.

[5] K. L. Kavanagh, *Semiconductor Science and Technology*, 2010, **25**, 024006.

[6] L. Cao, P. Fan, A. P. Vasudev, J. S. White, Z. Yu, W. Cai, J. A. Schuller, S. Fan and M. L. Brongersma, *Nano Letters*, 2010, **10**, 439–445.

[7] P. Krogstrup, H. I. Jørgensen, M. Heiss, O. Demichel, J. V. Holm, M. Aagesen, J. Nygard and A. Fontcuberta i Morral, *Nature Photonics*, 2013, **7**, 306–310.

[8] R. R. Lapierre, A. C. Chia, S. J. Gibson, C. M. Haapamaki, J. Boulanger, R. Yee, P. Kuyanov, J. Zhang, N. Tajik, N. Jewell and K. M. Rahman, *Physica Status Solidi - Rapid Research Letters*, 2013, **7**, 815–830.

[9] R. R. Lapierre, *Journal of Applied Physics*, 2011, **110**, 014310.

[10] W. Kim, L. Güniat, A. Fontcuberta I Morral and V. Piazza, *Applied Physics Reviews*, 2021, **8**, 011304.

[11] G. Mariani, A. C. Scofield, C.-H. Hung and D. L. Huffaker, *Nature Communications*, 2013, **4**, 1497.

[12] M. Yao, N. Huang, S. Cong, C.-Y. Chi, M. A. Seyedi, Y.-T. Lin, Y. Cao, M. L. Povinelli, P. D. Dapkus and C. Zhou, *Nano Letters*, 2014, **14**, 3293–3303.

[13] I. Aberg, G. Vescovi, D. Asoli, U. Naseem, J. P. Gilboy, C. Sundvall, A. Dahlgren, K. E. Svensson, N. Anttu, M. T. Bjork and L. Samuelson, *IEEE Journal of Photovoltaics*, 2016, **6**, 185–190.

[14] J. P. Boulanger, A. C. Chia, B. Wood, S. Yazdi, T. Kasama, M. Aagesen and R. R. LaPierre, *IEEE Journal of Photovoltaics*, 2016, **6**, 661–667.

[15] A. Mukherjee, D. Ren, P.-E. Vullum, J. Huh, B.-O. Fimland and H. Weman, *ACS Photonics*, 2021, **8**, 2355–2366.

[16] M. Yao, S. Cong, S. Arab, N. Huang, M. L. Povinelli, S. B. Cronin, P. D. Dapkus and C. Zhou, *Nano Letters*, 2015, **15**, 7217–7224.

[17] B. Feuerbacher and P. Wurfel, *Journal of Physics: Condensed Matter*, 1990, **2**, 3803–3810.

[18] A. Delamarre, L. Lombez and J. F. Guillemoles, *Applied Physics Letters*, 2012, **100**, 131108.

[19] K. Schick, E. Daub, S. Finkbeiner and P. Würfel, *Applied Physics A Solids and Surfaces*, 1992, **54**, 109–114.

[20] G. Smestad and H. Ries, *Solar Energy Materials and Solar Cells*, 1992, **25**, 51–71.

[21] V. D. Rumyantsev and J. A. Rodriguez, *Solar Energy Materials and Solar Cells*, 1993, **31**, 357–370.

[22] G. H. Bauer, R. Brüggemann, S. Tardon, S. Vignoli and R. Kniese, *Thin Solid Films*, 2005, **480-481**, 410–414.

[23] T. Trupke, R. A. Bardos, M. D. Abbott and J. E. Cotter, *Applied Physics Letters*, 2005, **87**, 093509.

[24] A. DELAMARRE, *PhD thesis*, Université Pierre et Marie Curie, 2013.

[25] J. E. M. Haverkort, E. C. Garnett and E. P. A. M. Bakkers, *Applied Physics Reviews*, 2018, **5**, 031106.

[26] Y. H. Kim, D. W. Park and S. J. Lee, *Applied Physics Letters*, 2012, **100**, 033117.

[27] M. H. T. Dastjerdi, J. P. Boulanger, P. Kuyanov, M. Aagesen and R. R. LaPierre, *Nanotechnology*, 2016, **27**, 475403.

[28] F. Panciera, Z. Baraissov, G. Patriarche, G. Vladimir, F. Glas, L. Travers, U. Mirsaidov, J. Christophe, F. Panciera, Z. Baraissov, G. Patriarche, V. G. Dubrovskii and F. Glas, *Nano Letters*, 2020, **20**, 1669–1675.

[29] S. Plissard, G. Larrieu, X. Wallart and P. Caroff, *Nanotechnology*, 2011, **22**, 275602.

[30] E. Russo-Averchi, M. Heiss, L. Michelet, P. Krogstrup, J. Nygard, C. Magen, J. R. Morante, E. Uccelli, J. Arbiol and A. Fontcuberta i Morral, *Nanoscale*, 2012, **4**, 1486.

[31] F. Bastiman, H. Küpers, C. Somaschini and L. Geelhaar, *Nanotechnology*, 2016, **27**, 095601.

[32] F. Matteini, G. Tütüncüoglu, D. Mikulik, J. Vukajlovic-Plestina, H. Potts, J. B. Leran, W. C. Carter and A. F. Morral, *Crystal Growth and Design*, 2016, **16**, 5781–5786.

[33] M. Zamani, G. Tütüncüoglu, S. Martí-Sánchez, L. Francaviglia, L. Güniat, L. Ghisalberti, H. Potts, M. Friedl, E. Markov, W. Kim, J. B. Leran, V. G. Dubrovskii, J. Arbiol and A. Fontcuberta I Morral, *Nanoscale*, 2018, **10**, 17080–17091.

[34] J. Vukajlovic-Plestina, W. Kim, L. Ghisalberti, G. Varnavides, G. Tütüncuoglu, H. Potts, M. Friedl, L. Güniat, W. C. Carter, V. G. Dubrovskii and A. Fontcuberta i Morral, *Nature Communications*, 2019, **10**, 869.

[35] A. Scaccabarozzi, A. Cattoni, G. Patriarche, L. Travers, S. Collin, J.-C. Harmand, F. Glas and F. Oehler, *Nanoscale*, 2020, **12**, 18240–18248.

[36] D. Bahrami, S. M. Mostafavi Kashani, A. Al Hassan, A. Davtyan and U. Pietsch, *Nanotechnology*, 2020, **31**, 185302.

[37] D. P. Wilson, V. G. Dubrovskii and R. R. LaPierre, *Nanotechnology*, 2021, **32**, 265301.

[38] R. D. Lépinau, *PhD thesis*, Université Paris-Saclay, 2020.

[39] S. A. Dayeh, R. Chen, Y. G. Ro and J. Sim, *Materials Science in Semiconductor Processing*, 2017, **62**, 135–155.

[40] M. H. T. Dastjerdi, E. M. Fiordaliso, E. D. Leshchenko, A. Akhtari-Zavareh, T. Kasama, M. Aagesen, V. G. Dubrovskii and R. R. LaPierre, *Nano Letters*, 2017, **17**, 5875–5882.

[41] H.-L. Chen, C. Himwas, A. Scaccabarozzi, P. Rale, F. Oehler, A. Lemaitre, L. Lombez, J.-F. Guillemoles, M. Tchernycheva, J.-C. Harmand, A. Cattoni and S. Collin, *Nano Letters*, 2017, **17**, 6667–6675.

[42] T. Hakkarainen, M. R. Piton, E. M. Fiordaliso, E. D. Leshchenko, S. Koelling, J. Bettini, H. Vinicius, A. Galeti, E. Koivusalo, Y. G. Gobato, A. D. G. Rodrigues, D. Lupo, P. M. Koenraad, E. R. Leite, V. G. Dubrovskii and M. Guina, *Physical Review Materials*, 2019, **3**, 086001.

[43] C. Tong, T. Bidaud, E. Koivusalo, M. Rizzo Piton, M. Guina, H. V. A. Galeti, Y. Galvão Gobato, A. Cattoni, T. Hakkarainen and S. Collin, *Nanotechnology*, 2022, **33**, 185704.

[44] M. Hilse, M. Ramsteiner, S. Breuer, L. Geelhaar and H. Riechert, *Applied Physics Letters*, 2010, **96**, 193104.

[45] B. Ketterer, E. Mikheev, E. Uccelli and A. Fontcuberta I Morral, *Applied Physics Letters*, 2010, **97**, 223103.

[46] H. L. Chen, R. De Lépinau, A. Scaccabarozzi, F. Oehler, J. C. Harmand, A. Cattoni and S. Collin, *Physical Review Applied*, 2021, **15**, 024007.

[47] L. Ouattara, A. Mikkelsen, N. Sköld, J. Eriksson, T. Knaapen, E. Cavar, W. Seifert, L. Samuelson and E. Lundgren, *Nano Letters*, 2007, **7**, 2859–2864.
[48] S. Perera, M. A. Fickenscher, H. E. Jackson, L. M. Smith, J. M. Yarrison-Rice, H. J. Joyce, Q. Gao, H. H. Tan, C. Jagadish, X. Zhang and J. Zou, *Applied Physics Letters*, 2008, **93**, 053110.
[49] P. Parkinson, H. J. Joyce, Q. Gao, H. H. Tan, X. Zhang, J. Zou, C. Jagadish, L. M. Herz and M. B. Johnston, *Nano Letters*, 2009, **9**, 3349–3353.
[50] K. Tomioka, Y. Kobayashi, J. Motohisa, S. Hara and T. Fukui, *Nanotechnology*, 2009, **20**, 145302.
[51] O. Demichel, M. Heiss, J. Bleuse, H. Mariette and I. A. Fontcuberta Morral, *Applied Physics Letters*, 2010, **97**, 201907.
[52] C. C. Chang, C. Y. Chi, M. Yao, N. Huang, C. C. Chen, J. Theiss, A. W. Bushmaker, S. Lalumondiere, T. W. Yeh, M. L. Povinelli, C. Zhou, P. D. Dapkus and S. B. Cronin, *Nano Letters*, 2012, **12**, 4484–4489.
[53] K. J. Bachmann, H. Schreiber, W. R. Sinclair, P. H. Schmidt, F. A. Thiel, E. G. Spencer, G. Pasteur, W. L. Feldmann and K. Sreeharsha, *Journal of Applied Physics*, 1979, **50**, 3441–3446.
[54] N. Balasubramanian and A. Subrahmanyam, *Semiconductor Science and Technology*, 1990, **5**, 871–876.
[55] D. V. Morgan, Y. Aliyu and R. W. Bunce, *Physica Status Solidi (a)*, 1992, **133**, 77–93.
[56] C. T. Lee, C. H. Fu, C. D. Tsai and W. Lin, *Journal of Electronic Materials*, 1998, **27**, 1017–1021.
[57] R. De Lepinau, C. Tong, A. Scaccabarozzi, F. Oehler, H. L. Chen, B. Berenguier, A. Delamarre, S. Collin and A. Cattoni, 2020 47th IEEE Photovoltaic Specialists Conference (PVSC), 2020, pp. 1842–1845.
[58] H. L. Chen, A. Scaccabarozzi, R. D. Lepinau, F. Oehler, A. Lemaitre, J. C. Harmand, A. Cattoni and S. Collin, *Physical Review Applied*, 2021, **15**, 024006.
[59] J. P. Hugonin and P. Lalanne, *RETICOLO CODE 1D for the diffraction by stacks of lamellar 1D gratings (classical diffraction)*, Institut d'optique/cnrs technical report, 2005.
[60] P. Lalanne and G. M. Morris, *Journal of the Optical Society of America A.*, 1996, **13**, 779–784.
[61] L. Li, *Journal of the Optical Society of America A.*, 1997, **14**, 2758–2767.
[62] P. Lalanne and M. P. Jurek, *Journal of Modern Optics*, 1998, **45**, 1357–1374.
[63] Y. Cui, D. Van Dam, S. A. Mann, N. J. Van Hoof, P. J. Van Veldhoven, E. C. Garnett, E. P. Bakkers and J. E. Haverkort, *Nano Letters*, 2016, **16**, 6467–6471.
[64] D. Mikulik, M. Ricci, G. Tutuncuoglu, F. Matteini, J. Vukajlovic, N. Vulic, E. Alarcon-Llado and A. Fontcuberta i Morral, *Nano Energy*, 2017, **41**, 566–572.
[65] E. Barrigón, Y. Zhang, L. Hrachowina, G. Otnes and M. T. Borgström, *Nano Energy*, 2020, **71**, 104575.
[66] S. L. Howell, S. Padalkar, K. Yoon, Q. Li, D. D. Koleske, J. J. Wierer, G. T. Wang and L. J. Lauhon, *Nano Letters*, 2013, **13**, 5123–5128.
[67] H. Elanzeery, M. Melchiorre, M. Sood, F. Babbe, F. Werner, G. Brammertz and S. Siebentritt, *Physical Review Materials*, 2019, **3**, 55403.
[68] L. Lombez, M. Soro, A. Delamarre, N. Naghavi, N. Barreau, D. Lincot and J. F. Guillemoles, *Journal of Applied Physics*, 2014, **116**, 064504.
[69] M. Sood, A. Lumisco, F. Werner, A. Nikolaeva, P. Dale, M. Melchiorre, J. Guillot, D. Abou-Ras and S. Siebentritt, *Solar RRL*, 2021, **5**, 2100078.
[70] M. Stolterfoht, P. Caprioglio, C. M. Wolff, J. A. Márquez, J. Nordmann, S. Zhang, D. Rothhardt, U. Hörmann, Y. Amir, A. Redinger, L. Kegelmann, F. Zu, S. Albrecht, N. Koch, T. Kirchartz, M. Saliba, T. Unold and D. Neher, *Energy and Environmental Science*, 2019, **12**, 2778–2788.
[71] P. Parkinson, Y. H. Lee, L. Fu, S. Breuer, H. H. Tan and C. Jagadish, *Nano Letters*, 2013, **13**, 1405–1409.
[72] D. Abou-Ras, T. Kirchartz and U. Rau, *Advanced Characterization Techniques for Thin Film Solar Cells: Second Edition*, Wiley-VCH, 2016, vol. 1-2, pp. 1–681.
[73] R. Scheer and H.-W. Schock, *Chalcogenide Photovoltaics*, Wiley-VCH, 2011, ch. 2.6.
[74] B. M. Kayes, H. Nie, R. Twist, S. G. Spruytte, F. Reinhardt, I. C. Kizilyalli and G. S. Higashi, *2011 37th IEEE Photovoltaic Specialists Conference*, 2011, 000004–000008.
[75] A. S. Gudovskikh, K. S. Zelentsov, A. I. Baranov, D. A. Kudryashov, I. A. Morozov, E. V. Nikitina and J. P. Kleider, *Energy Procedia*, 2016, **102**, 56–63.
[76] M. Burgelman, P. Nollet and S. Degrave, *Thin Solid Films*, 2000, **361**, 527–532.
[77] O. Supplie, M. M. May, G. Steinbach, O. Romanyuk, F. Grosse, A. Nägelein, P. Kleinschmidt, S. Brückner and T. Hannappel, *Journal of Physical Chemistry Letters*, 2015, **6**, 464–469.
[78] R. Roychowdhury, S. Kumar, A. Wadikar, C. Mukherjee, K. Rajiv, T. K. Sharma and V. K. Dixit, *Applied Surface Science*, 2017, **419**, 957–967.
[79] Ioffe Institute, *New Semiconductor Materials. Characteristics and Properties*.
[80] M. Levinshtein, S. Rumyqntsev and M. Shur, *Handbook series on semiconductor parameters*, World Scientific, 1999.
[81] M. O. Gomez, *PhD thesis*, Universidad Politécnica de Madrid, Escuela Técnica Superior de Ingenieros de Telecomunicación, 2018.
[82] Y. C. Kao, H. M. Chou, S. C. Hsu, A. Lin, C. C. Lin, Z. H. Shih, C. L. Chang, H. F. Hong and R. H. Horng, *Scientific Reports*, 2019, **9**, 4308.

A. Characterization of as-grown NW arrays

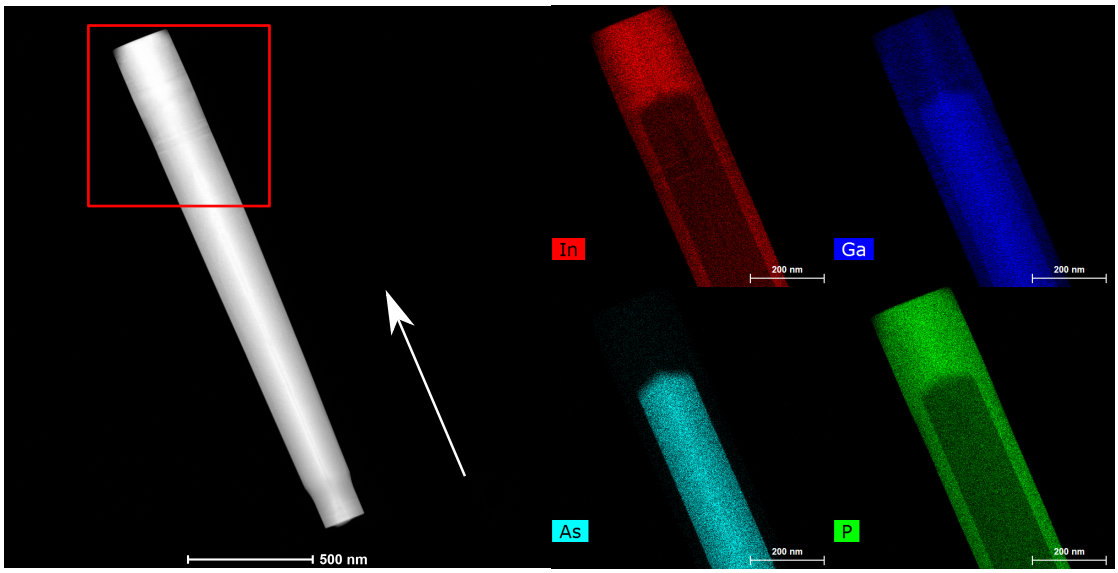

Figure 6 (left) Scanning transmission electron microscopy (STEM) image taken with a high-angle annular dark field (HAADF) detector. The white arrow indicates the GaAs [111]B growth direction. (right) Corresponding In, Ga, As, and P elemental maps of the final NW section, indicated by the red square in the STEM-HAADF image, obtained by energy dispersive X-ray analysis (EDX). The core-shell heterostructure can be seen from the $\langle 11\bar{2} \rangle$ zone-axis.

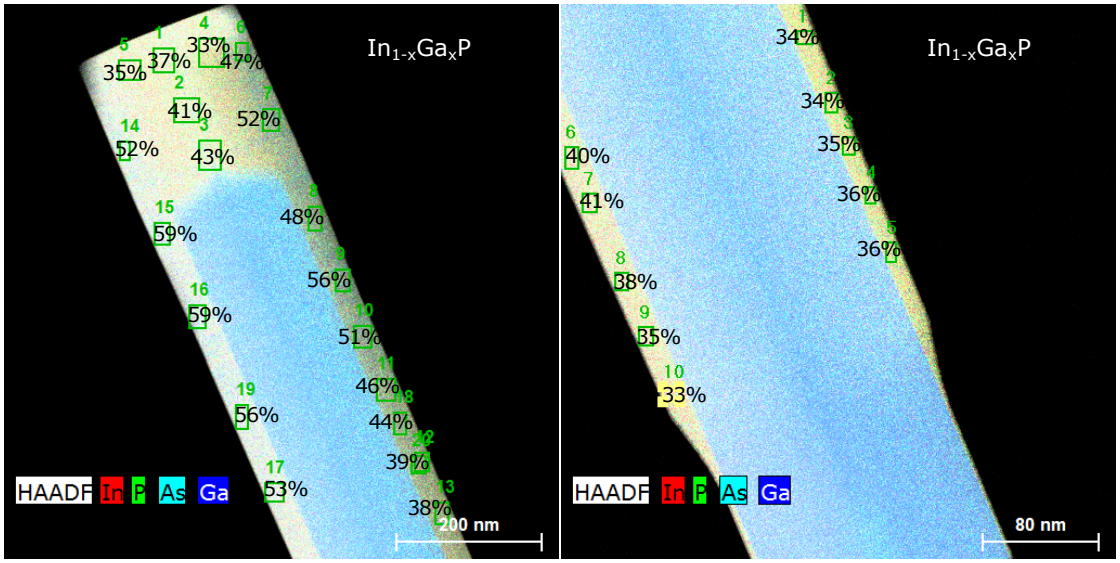

Figure 7 Combination image assembled from the HAADF image (black and white) and the corresponding In, Ga, As, P, elemental EDX maps (colour). The values indicated in percentage are the chemical composition parameter x of the $In_{1-x}Ga_xP$ shell for each selected zones (green rectangles). Left image is an overview of the final NW section, right image shows the bottom of the NW.

B. Electrical performances of other NW solar cells from the same sample

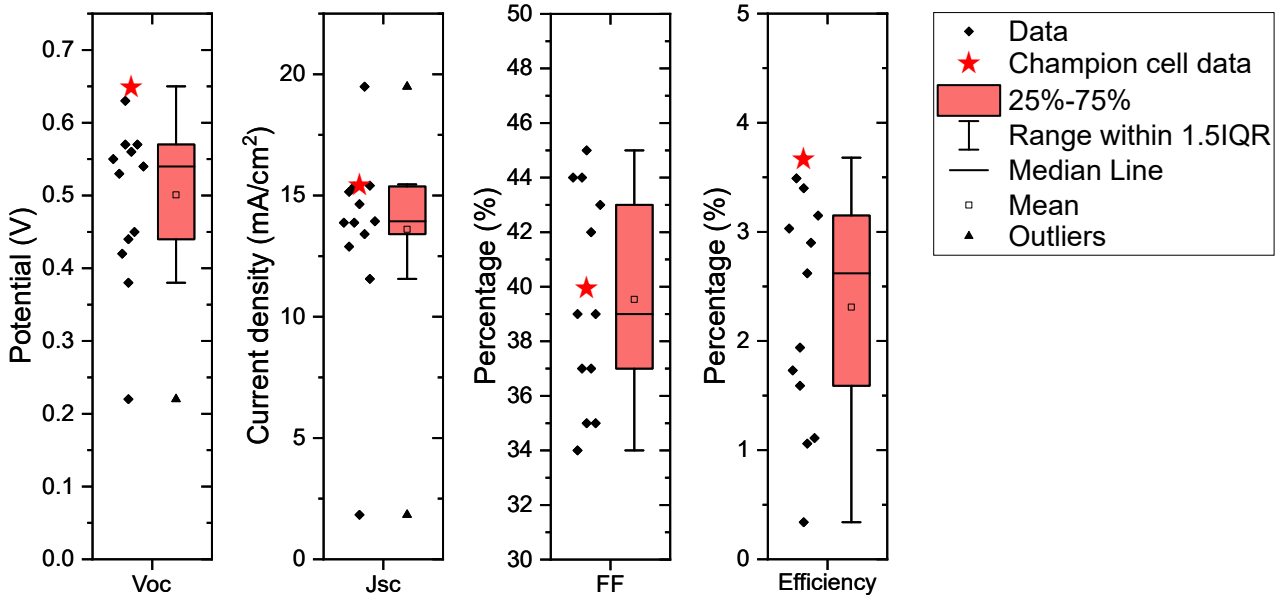

Figure 8 Box plots showing the V_{OC}, J_{SC}, FF and efficiency measurements for 13 NW solar cells from the same sample. The cell investigated in-depth in the article corresponds to the champion cell, whose performances are indicated by the red stars ($V_{OC} = 0.65$ V, $J_{SC} = 15.5$ mA/cm^2, FF $= 40$ %, $\eta = 3.7$ %). A J_{SC} value of 14.2 mA/cm^2 is put forward in the main article as it is the one obtained by integrating the EQE curve in Figure 3c (see section 3.1).

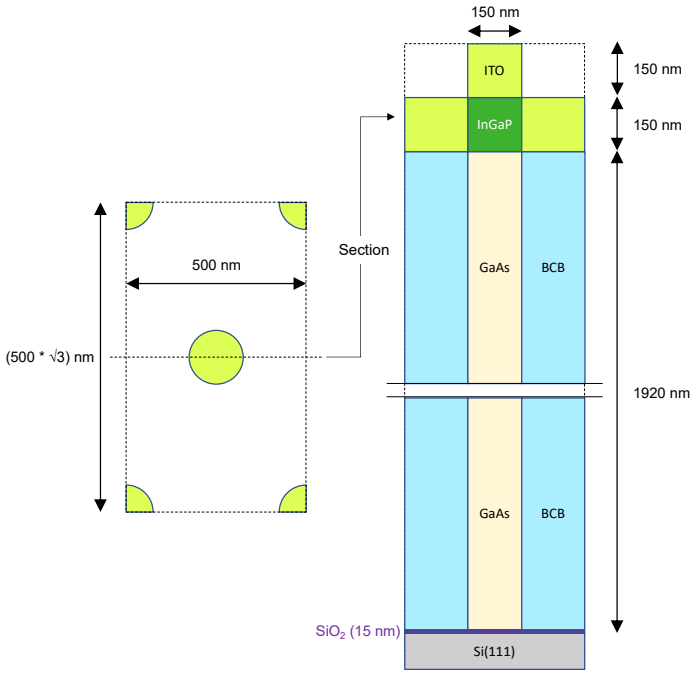

Figure 9 Schematics of the NW solar cell used in the RCWA simulations. (left) A top view of the unit cell (hexagonal) composing the NW array. (right) A cross-section view of the NW solar cell along a single NW. The simulation results are presented in Figure 3c.

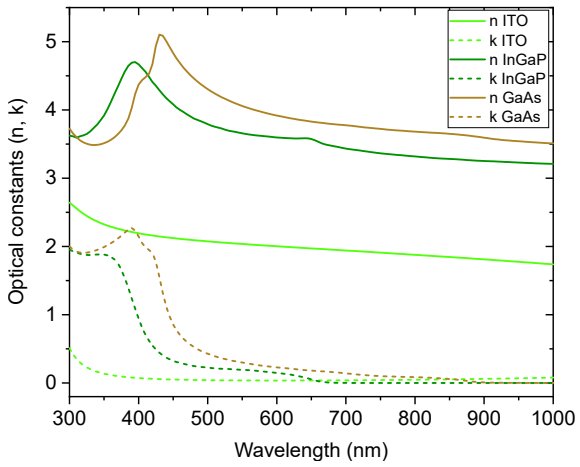

Figure 10 Refractive indices (n) and extinction coefficients (k) used in absorption simulations carried out using the RCWA method.

C. NW absorption simulations

D. Hyperspectral PL and qFl splitting maps

From Figures 11c and 11d, quasi-Fermi level splitting variations of $\pm$ 20 meV and $\pm$ 25 meV can be observed respectively for the 12 suns and 81 suns PL measurements. This demonstrates the relatively high qFl splitting homogeneity over the characterized device surface.

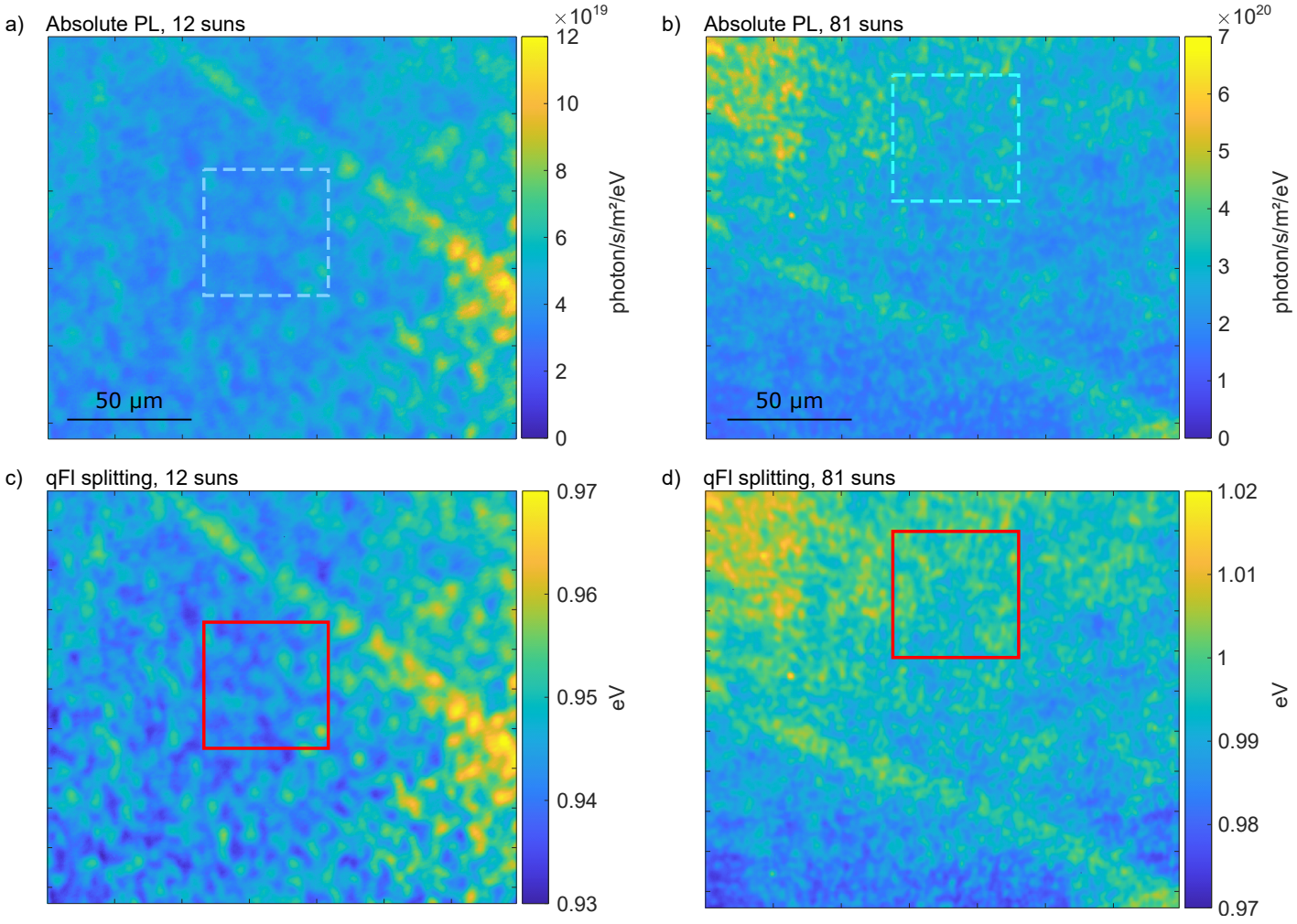

Figure 11 Hyperspectral PL maps of the champion NW cell emission at 870 nm (1.43 eV) calibrated in absolute units, under an illumination of (a) 12 suns and (b) 81 suns. (c) and (d) show the qFl splitting maps of the same areas obtained by fitting the PL spectra using the generalized Planck law (equation 2) between 1.43 and 1.52 eV with a fixed carrier temperature of 330 K.

Table I Parameters used in the 1D SCAPS simulations presented in Figure 5. The material parameters were extracted from references [79–82]. The acceptor doping concentration in p-GaP (in bold in the table) was varied between 1 x 10^{18} and 8 x 10^{18} cm^{-3} in the SCAPS simulations.

	p-Si	p-GaP	Graded GaP/GaAs	p-GaAs	i-GaAs	n-GaInP	n^+-GaInP
Thickness (nm)	100	58	22	50	24	28	6
Bandgap (eV)	1.12	2.26	linearly graded	1.424	1.424	1.85	1.85
Electron affinity (eV)	4.05	3.8	linearly graded	4.07	4.07	4.01	4.01
Dielectric permittivity	11.9	11.1	linearly graded	12.9	12.9	11.8	11.8
CB effective density of states (cm^{-3})	2.8 x 10^{19}	1.8 x 10^{19}	linearly graded	4.7 x 10^{17}	4.7 x 10^{17}	6.24 x 10^{17}	6.24 x 10^{17}
VB effective density of states (cm^{-3})	1.04 x 10^{19}	1.9 x 10^{19}	linearly graded	9 x 10^{18}	9 x 10^{18}	1.46 x 10^{19}	1.46 x 10^{19}
Electron thermal velocity (cm/s)	2.3 x 10^7	2 x 10^7	linearly graded	4.4 x 10^7	4.4 x 10^7	3.9 x 10^7	3.9 x 10^7
Hole thermal velocity (cm/s)	1.65 x 10^7	1.3 x 10^7	linearly graded	1.8 x 10^7	1.8 x 10^7	1.4 x 10^7	1.4 x 10^7
Electron mobility (cm^2.V.s)	1.5 x 10^3	2.5 x 10^2	linearly graded	8.5 x 10^3	8.5 x 10^3	5.0 x 10^2	5.0 x 10^2
Hole mobility (cm^2.V.s)	4.5 x 10^2	1.5 x 10^2	linearly graded	4.0 x 10^2	4.0 x 10^2	30	30
Doping concentration (cm^{-3})	(p) 1.0 x 10^{19}	**(p) 1.0 x 10^{18}**	linearly graded	(p) 3.0 x 10^{18}	(n residual) 1.0 x 10^{15}	(n) 1.0 x 10^{18}	(n) 1.0 x 10^{19}
Radiative recombination coeff. (cm^3/s)	1.0 x 10^{-15}	1.0 x 10^{-13}	linearly graded	2.0 x 10^{-10}	2.0 x 10^{-10}	1 x 10^{-10}	1 x 10^{-10}
Auger electron capture coeff. (cm^6/s)	3.0 x 10^{-31}	0	linearly graded	5.0 x 10^{-30}	5.0 x 10^{-30}	4.7 x 10^{-30}	4.7 x 10^{-30}
Auger hole capture coeff. (cm^6/s)	3.0 x 10^{-31}	0	linearly graded	1.0 x 10^{-31}	1.0 x 10^{-31}	1.1 x 10^{-30}	1.1 x 10^{-30}

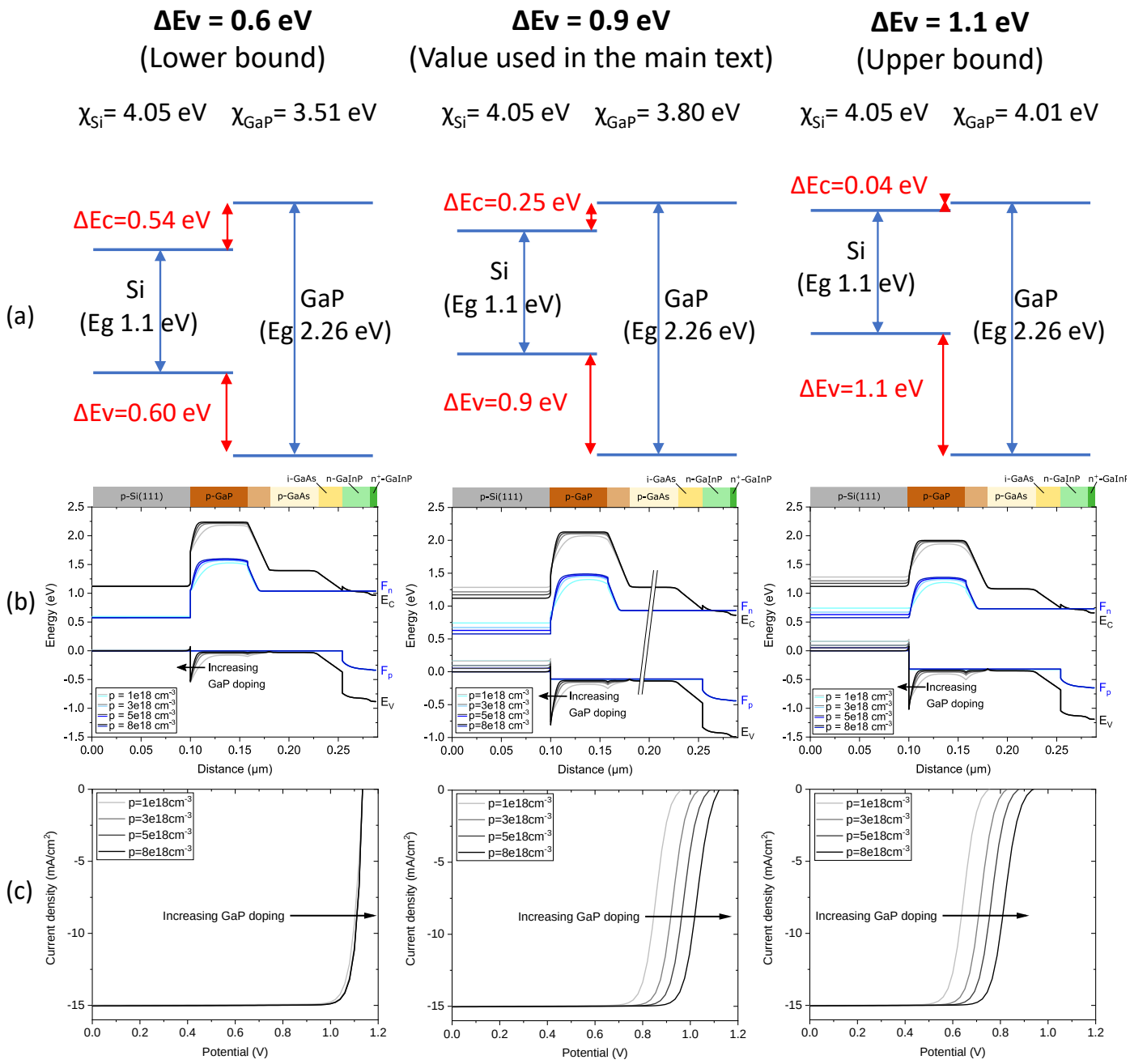

(d)

	ΔEv = 0.6 eV				ΔEv = 0.9 eV				ΔEv = 1.1 eV			
	Voc (V)	Jsc (mA/cm²)	FF (%)	η (%)	Voc (V)	Jsc (mA/cm²)	FF (%)	η (%)	Voc (V)	Jsc (mA/cm²)	FF (%)	η (%)
p=1x10^{18} cm^{-3}	1.14	15.0	87.6	14.9	0.96	15.0	77.0	11.1	0.75	15.0	71.8	8.1
p=3x10^{18} cm^{-3}	1.14	15.0	88.7	15.1	1.03	15.0	78.0	12.1	0.83	15.0	73.4	9.1
p=5x10^{18} cm^{-3}	1.14	15.0	88.8	15.2	1.08	15.0	78.7	12.8	0.88	15.0	74.1	9.8
p=8x10^{18} cm^{-3}	1.14	15.0	88.9	15.2	1.12	15.0	80.6	13.6	0.94	15.0	74.9	10.6

Figure 12 Impact of the VB offset (ΔE_V) at the GaP/Si interface on the SCAPS simulation results. (a) Comparison between the lower and upper bound GaP/Si VB offset values found in the literature (ΔE_V=0.6 eV[77] and ΔE_V=1.1 eV[78], respectively) and the average value of 0.9 eV used in the simulations presented in the main article. The corresponding electron affinities for Si and GaP (χ_{Si} and χ_{GaP}) are also indicated. (b) Band diagrams obtained from 1D SCAPS simulations under 1 sun illumination and V_{MPP} bias for different GaP acceptor doping concentrations. (c) Corresponding current-voltage characteristics under 1 sun illumination. The figures of merit V_{OC}, J_{SC}, FF, and η are summarized in table (d).